

# Reversible Li-Ion Conversion Reaction for a $Ti_xGe$ Alloy in a Ti/Ge Multilayer

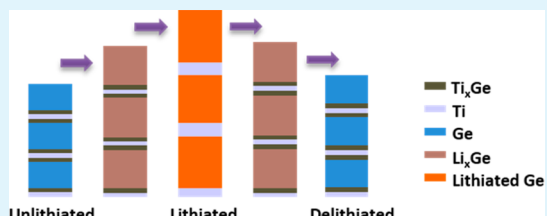
Xiao Chen,<sup>†,‡</sup> Tim T. Fister,<sup>†</sup> Jennifer Esbenshade,<sup>§</sup> Bing Shi,<sup>†</sup> Xianyi Hu,<sup>‡</sup> Jinsong Wu,<sup>‡</sup> Andrew A. Gewirth,<sup>§</sup> Michael J. Bedzyk,<sup>‡,¶</sup> and Paul Fenter<sup>\*,†,¶</sup>

<sup>†</sup>Chemical Sciences and Engineering Division, Argonne National Laboratory, Lemont, Illinois 60439, United States

<sup>‡</sup>Applied Physics Program and Materials Science and Engineering Department, Northwestern University, Evanston, Illinois 60208, United States

<sup>§</sup>Chemistry Department, University of Illinois Urbana–Champaign, Champaign, Illinois 61801, United States

**ABSTRACT:** Group IV intermetallics electrochemically alloy with Li with stoichiometries as high as  $Li_{4.4}M$  ( $M = Si, Ge, Sn, or Pb$ ). This provides the second highest known specific capacity (after pure lithium metal) for lithium-ion batteries, but the dramatic volume change during cycling greatly limits their use as anodes in Li-ion batteries. We describe an approach to overcome this limitation by constructing electrodes using a Ge/Ti multilayer architecture. *In operando* X-ray reflectivity and *ex situ* transmission electron microscopy are used to characterize the heterolayer structure at various lithium stoichiometries along a lithiation/delithiation cycle. The as-deposited multilayer spontaneously forms a one-dimensional  $Ti_xGe/Ti/Ti_xGe$  core–shell planar structure embedded in a Ge matrix. The interfacial  $Ti_xGe$  alloy is observed to be electrochemically active and exhibits reversible phase separation (i.e., a conversion reaction). Including the germanium components, the overall multilayer structure exhibits a 2.3-fold reversible vertical expansion and contraction and is shown to have improved capacity and capacity retention with respect to a Ge film with equivalent active material thickness.



**KEYWORDS:** *Li-ion battery, germanium, thin film, multilayer, X-ray reflectivity, Patterson function, Ge/Ti alloy*

## INTRODUCTION

Electronic mobile devices and electrical vehicles rely on increased energy capacity and power of batteries. Carbonaceous materials have been the primary choice for anodes in commercial Li-ion batteries for decades, primarily relying on intercalation in graphite to form  $LiC_6$ . In comparison, conversion materials have much higher specific capacity, especially group IV intermetallics (4200 mAh/g for silicon and 1620 mAh/g for germanium compared to 372 mAh/g for  $LiC_6$ ). However, the intrinsically large volume change during cycling of group IV intermetallics (typically ~4-fold expansion) is problematic as it pulverizes the active materials, causing delamination from the current collector and conductive binders that leads to Li trapping and severe capacity fade. One common approach for solving this problem is to reduce the size of the electrode material structure to the nanoscale, such as forming thin films,<sup>1,2</sup> nanoparticles,<sup>3,4</sup> mesoporous films,<sup>5,6</sup> and nanoarrays.<sup>7</sup> Such systems are designed to reduce overall strain and improve transport properties but often suffer from poor Coulombic efficiency due to side reactions that scale with surface area.

Previously, it was demonstrated that multilayers consisting of alternating thin films of amorphous silicon and conducting adhesive metal layers allowed the intrinsically high Li capacity of silicon to be combined with the reversibility of ultrathin silicon films and the conductivity of a composite material while maintaining a high Coulombic efficiency.<sup>8–10</sup> Though Si is

favored over other group IV elements, due to its high capacity, low cost, and abundance, Ge is attractive due to its intrinsically high electronic conductivity at room temperature (2.1 S/m), which is 3 orders of magnitude higher than that of Si ( $1.6 \times 10^{-3}$  S/m).<sup>11</sup> Also, Li diffusivity in Ge ( $6.25 \times 10^{-12}$  cm<sup>2</sup>/s) is 2 orders of magnitude higher than Si ( $1.9 \times 10^{-14}$  cm<sup>2</sup>/s).<sup>12</sup> These electronic and ionic transport properties make Ge electrodes more suitable for high power anodes. Ge also benefits from its minimal surface native oxide, in contrast to silicon,<sup>1</sup> that reacts with Li during the initial charging to form  $Li_2O$ . This can lead to a large irreversible capacity for the first cycle for nanostructured anodes that have intrinsically large surface areas.

Here, the lithiation of sputter-deposited Ge/Ti multilayer films were studied as a model nanostructured anode. Transmission electron microscopy (TEM) images and X-ray reflectivity (XRR) data (using a Patterson function analysis) clearly show the development of  $Ti_xGe$  alloy<sup>13</sup> formation at the Ti–Ge interfaces within the as-deposited film. *In operando* XRR measurements observed that  $Ti_xGe$  alloy layers are electrochemically active and exhibit a reversible conversion reaction to titanium plus lithiated germanium during lithiation/delithiation reactions. That is, the  $Ti_xGe$  framework acts both as a binding

Received: November 17, 2016

Accepted: February 13, 2017

Published: February 13, 2017

material that prevents Ge layers from delaminating when undergoing the extremely large volume changes during lithiation reactions and also as an active material for lithiation. This creates a hybrid electrode chemistry in which the lithiation of the Ge layers is a simple alloying reaction, while the lithiation of the  $Ti_xGe$  layers involves reversible phase segregation (e.g., a conversion reaction) leading to Ti layers and lithiated Ge. The results are discussed in the context of *in operando* X-ray analysis at different stages of lithiation/delithiation.

## EXPERIMENTAL DETAILS

**Sample Fabrication and Testing.** Ge/Ti multilayers were deposited using dc magnetron sputtering. The rotary magnetron sputtering system was customized with two sputtering targets set horizontally. The base pressure was  $5 \times 10^{-7}$  Torr, the deposition pressure was 2.3 mTorr of Ar, and the power for both targets was 215 W. Target masks were designed to achieve uniform films. The growth rate was calibrated using XRR. The Ge/Ti multilayers were deposited on fused quartz at room temperature by translating the substrate holder between the Ti and Ge targets to grow alternating layers of 20 Ti/Ge bilayers, with a bottom layer of Ti and a top layer of Ge. The sample used for XRR measurements had nominal film thicknesses of 20 Å Ti and 100 Å Ge, while that for the TEM results were 50 Å Ti and 100 Å Ge. Galvanostatic measurements of the extended electrochemical cycling performance of the Ge/Ti multilayers were tested at a 1 C rate (using a multichannel Arbin cycler) to probe the stability and performance of a 20 period multilayer with 100 Å Ge and 40 Å Ti layer thicknesses and is compared to a thin Ge film with the same overall thickness (2000 Å).

**Transmission Electron Microscopy.** The cross-sectional TEM samples were prepared by a FEI Helios focused ion beam (FIB). After the thin section has been mounted on a FIB-grid, it is transferred into a TEM. The Ge/Ti multilayers thin film was then studied by a JEOL-2100F transmission electron microscope at 200 kV. High-resolution electron microscopy (HREM) images showing phase contrast were taken to study the interface structure.

**X-ray Reflectivity Measurements.** *In operando* XRR measurements were performed at 33BM-C of the Advanced Photon Source (APS) in Argonne National Laboratory (ANL) using an X-ray photon energy of 20.00 keV with an incident flux of  $\sim 10^{10}$  photons/s. The X-ray beam (with cross section of  $2 \times 0.2$  mm<sup>2</sup> and divergence of 40  $\mu\text{rad} = 0.0005 \text{ \AA}^{-1}$  along  $2\theta$  direction) illuminated a 2 mm wide by 3 mm long area on the sample. A specially designed transmission electrochemistry cell<sup>8,14</sup> was used to study the multilayer samples as a function of applied electrochemical potential. The sample size is 10 mm wide and 3 mm along the X-ray beam direction. The electrochemical potential of the working electrode and its associated currents were controlled by a CHI760D potentiostat. Li metal was used as both the counter and reference electrodes forming a half-cell, and all potentials are reported versus the Li/Li<sup>+</sup> redox couple. Data were collected at fine intervals ( $\Delta q = 0.001 \text{ \AA}^{-1}$ ) using an area detector (Pilatus 100k). Each XRR scan took 5 min. In the present data, the statistical uncertainties in the experimental data are smaller than the systematic errors (e.g., associated with inhomogeneities in the sample thickness, for instance, as evidenced by the lack of Kiessig fringes), and therefore we have assigned a nominal and uniform relative uncertainty of 2% for each data point.

**X-ray Reflectivity and Patterson Function Analysis.** Thin film X-ray reflectivity directly probes the vertical (i.e., laterally averaged) electron density profile of heterolayer structures, both within the layers and at the interfaces.<sup>9,15–19</sup> Specifically, the X-ray reflectivity signal,  $R(Q)$ , is the fraction of the X-ray beam that is reflected from the surface as a function of the angle of incidence,  $\theta$ , of the X-ray beam. For specular reflection, the scattering condition is characterized by a scattering vector magnitude,  $Q = 4\pi \sin(\theta)/\lambda$ , where  $\lambda$  is the X-ray wavelength. XRR is directly sensitive to the thickness, density, and interface roughness of interfaces in a multilayer structure. For simplicity, we limit the measurements to the kinematical regime,

where the reflectivity  $R \ll 1$ , corresponding to  $Q > 3Q_c$ , where  $Q_c$  is the scattering vector at the critical angle for total external reflection.<sup>17</sup> A simplification of the analysis of XRR data is obtained by normalizing the measured XRR signal by that of the calculated Fresnel reflectivity,  $R_F(Q)$ , corresponding to a bare substrate crystal. Here, the normalized XRR signal ( $nR$ ) from a multilayer structure with electron density profile  $\rho(z)$  can be expressed as<sup>20</sup>

$$nR(Q) = \frac{R(Q)}{R_F(Q)} = \left| \int_{-\infty}^{\infty} \frac{d\rho(z)}{dz} e^{iQz} dz \right|^2 \quad (1)$$

where the Fresnel reflectivity from the substrate can be written as

$$R_F \cong \left( 2 \frac{Q}{Q_c} \right)^{-4} \quad (2)$$

Analysis of XRR data for extended multilayer structures can be challenging, especially when each of the 20 repeated layer pairs may not be precisely identical. Such a structural analysis requires a model with more than 60 parameters to describe the structure at every state of charge. This challenge can be addressed with a model-independent Patterson function analysis to define the changes in the multilayer structure during lithiation reactions directly from the data. For the specific case of XRR data in the Fresnel regime, the 1D Patterson function,  $P(\Delta z)$ , is defined, using Parseval's theorem, from the Fourier transform of the Fresnel-normalized reflectivity.<sup>21</sup>

$$\begin{aligned} P(\Delta z) &= FT \left( \frac{R(Q)}{R_F(Q)} \right) = \frac{1}{2\pi} \int FT(\rho'(z)) FT^*(\rho'(z)) e^{-iQz} dQ \\ &= \rho'(z) \otimes \rho'(-z) \end{aligned} \quad (3)$$

That is, the Patterson function corresponds to the autocorrelation of the electron density gradient,  $\rho'(z)$ , and can be obtained directly by a numerical Fourier transformation of the data (without any special considerations, such as a window function associated with the termination of the data range). In the limit of a stepwise electron density profile (i.e., as appropriate to a multilayer structure), each interface in the density gradient,  $\rho'(z)$ , can be described by a Gaussian function defined by three parameters, corresponding to the interface position,  $z_0$ , an rms width,  $\sigma$  (describing the interface roughness), and the interfacial density contrast,  $\Delta\rho$ . Consequently, the Patterson function is described by a sum of Gaussian functions that represent the convolution of the contributions from separate interfaces associated with the interference between X-rays scattered at each interface described by separations  $z_i - z_j$  widths,  $(\sigma_i^2 + \sigma_j^2)^{1/2}$ , and magnitudes,  $\Delta\rho_i \Delta\rho_j$ , of the two interfaces ( $i$  and  $j$ ). Therefore, the Patterson function directly reveals the separations between sharp interfaces. Combining this with *a priori* knowledge of the layer-by-layer synthesis and TEM, we can determine a model for the electron density profile, even for a relatively complicated structure. Ultimately, the structural model derived from the insights from the Patterson function analysis can be optimized and quantified by a  $\chi^2$  optimization along with the parameter uncertainties. We note that since the Patterson function analysis involves interfacial electron density differences (rather than the electron densities of the films, themselves), uncertainties in the actual electron densities can be substantial (especially in the present measurements where the multilayer structure is very thick and there are no measurable Kiessig fringes, indicating that we do not have the substrate as an internal reference for electron densities). Consequently, our discussion emphasizes the structural changes in the sample rather than the changes in electron density.

An illustration of the Patterson function analysis for a simple two-layer multilayer is depicted in Figure 1. The simulated multilayer system consists of  $N_{ML} = 10$  periods of a 30 Å thick high density layer followed by a 50 Å thick low density layer on top of a semi-infinite substrate. It also shows the electron density profile for the first two bilayers of the multilayer, along with its derivative. The simulated X-ray reflectivity,  $R$ , from the entire multilayer structure (Figure 1b) includes Bragg peaks associated with the multilayer periodicity ( $Q = 2\pi/d_{ML}$ , where  $d_{ML} = 80 \text{ \AA}$ ) and high-frequency oscillations associated

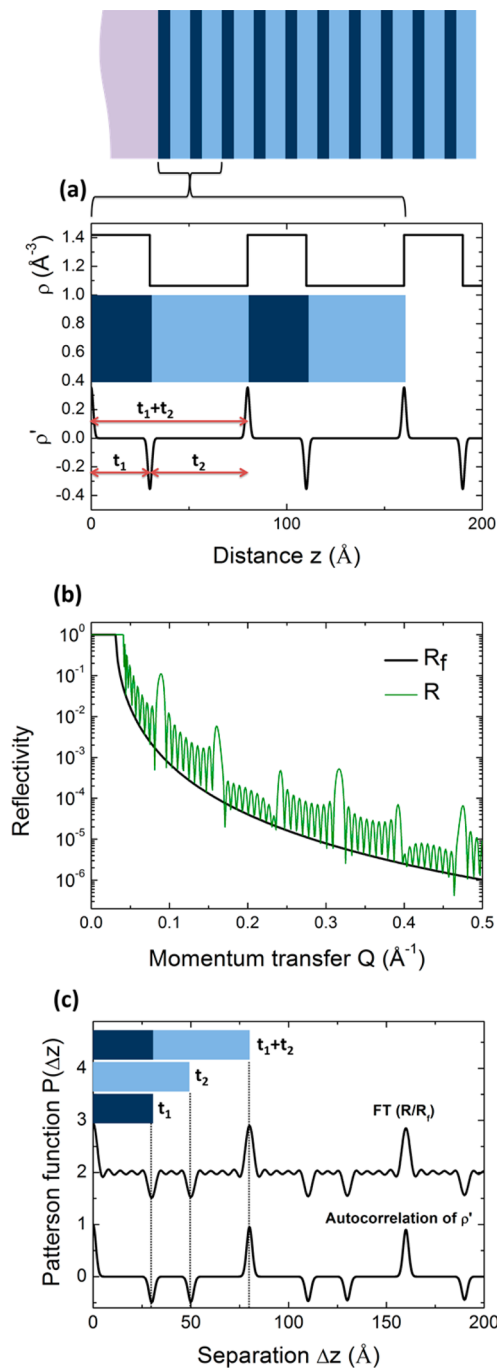


**Figure 1.** Patterson function simulation for an idealized periodic multilayer with  $N = 10$  periods grown on a substrate. (a) Multilayer model for simulation (direct view of this multilayer architecture, electron density profile for two bilayers and its derivative). (b) Simulated X-ray reflectivity,  $R$ , and Fresnel reflectivity of the substrate,  $R_F$ . (c) Comparison between the derived Patterson Function (by Fourier transform (FT) of the normalized X-ray reflectivity signal, calculated to  $Q = 1 \text{ \AA}^{-1}$ ) and the autocorrelation of the derivative of the electron density. The position of each peak within the first period of the Patterson function has been assigned to the associated film thickness.

with the total multilayer thickness (with a period of  $\delta Q = 2\pi/[N_{ML}d_{ML}]$ ). Also shown is the Fresnel reflectivity from the substrate,  $R_F$  (Figure 1b). The Patterson function (i.e., the Fourier transform of normalized X-ray reflectivity) is compared with the autocorrelation of the derivative of the electron density in Figure 1c, providing a graphical

demonstration of the validity of eq 3. Here, it can be seen that first three features in the Patterson function correspond to the thicknesses of the high-density layer (at 30  $\text{\AA}$ ), the low-density layer (at 50  $\text{\AA}$ ), and the multilayer period (at 80  $\text{\AA}$ ). Note that in this case the individual layer thicknesses appear as negative peaks while the multilayer period appears as a positive peak, since the sign of these features are due to the product of the interfacial density discontinuities associated with these features (i.e., negative peaks in  $P(z)$  are due to interference between interfaces with “up” and “down” density changes, while positive peaks are associated with two “up” or two “down” interfaces). Also seen in the derived Patterson function (Figure 1c) are small high-frequency oscillations with period  $2\pi/Q_{\max}$  that are due to the truncation of the  $Q$  range ( $0–1 \text{ \AA}^{-1}$ ) over which the Fourier transform was calculated.<sup>22</sup>

## RESULTS AND DISCUSSION

**Determination of the As-Deposited Ge/Ti Multilayer Structure.** The as-deposited multilayer film was characterized by transmission electron microscopy (TEM) (Figure 2) and X-

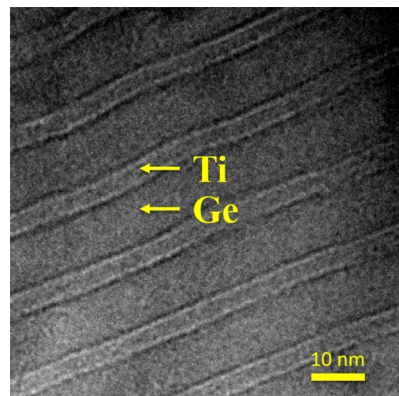


**Figure 2.** HREM image of the as-deposited Ge/Ti multilayer film. The contrast change is related to the electron density (darker areas correspond to higher electron densities).

ray reflectivity (Figure 3a). The TEM image clearly shows a well-defined periodic multilayer structure, as expected. The nominal film thicknesses from the TEM image are 40  $\text{\AA}$  for Ti and 100  $\text{\AA}$  for Ge, similar to that expected from the growth conditions. The image contrast is proportional to variations in the local electron density. Instead of the expected repeated bilayer structure with alternatively stacking between the Ge/Ti layers, it is apparent that the structure is more complex than expected. The TEM image has the appearance of a “pin-stripe” morphology, with a thin denser layer (dark) appearing at each interface between the Ge and Ti layers. This interfacial layer between the Ge and Ti layers is consistent with the formation of a higher density  $\text{Ti}_x\text{Ge}$  alloy layer.<sup>23</sup>

The X-ray reflectivity data show regular Bragg peaks associated with the multilayer structure, but without any evidence for the expected high-frequency oscillations associated with total film thickness (e.g., Kiessig fringes). This suggests that the multilayer structure and its morphology had a significant roughness. The derived Patterson function (Figure 3b) shows a more complex structure than expected for the multilayer with the simple bilayer substructure. Instead of the expected structure shown in Figure 1 with three distinct spacings within each period, the Patterson function of the Si/Ge structure has seven distinct intracell spacings. This is direct evidence that there are more than two layers in each unit multilayer period. The simplest multilayer structure consistent with the TEM image is one in which there are four layers within

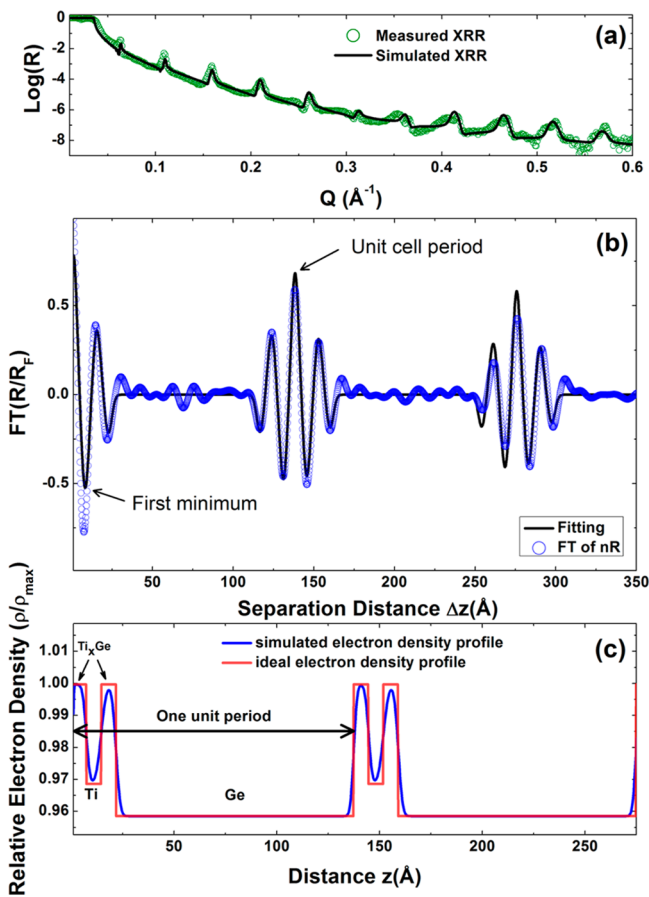


**Figure 3.** Patterson function analysis of the unlithiated multilayer. (a) Specular X-ray reflectivity data (green circle) of the unlithiated Ge/Ti multilayer sample and the calculated XRR signal (black line) using parameters obtained by fitting the observed Patterson function. (b) Calculated Patterson function (blue circle) for the as-deposited (unlithiated) state and its fitting curve (black line). (c) Idealized model of electron density profile (red line) and calculated electron density profile from the Patterson function analysis (blue line).

each unit period, corresponding to a core–shell structure embedded within a Ge matrix, fully consistent with the TEM images. Model fitting of the Patterson function gives the average thickness for each layer ( $7.2 \pm 0.1 \text{ \AA}$  for Ti layer,  $115.7 \pm 0.1 \text{ \AA}$  for Ge layer, and  $7.2 \pm 0.1 \text{ \AA}$  for an intervening  $\text{Ti}_x\text{Ge}$  alloy layer) revealing that the thicker layer seen in the TEM images corresponds to Ge. Simulated electron density profile from model fitting is shown in Figure 3c. This result is largely consistent with the intended deposition thicknesses ( $20 \text{ \AA}$  Ti and  $100 \text{ \AA}$  Ge). The simulated XRR signal, using fitted parameters (thickness, roughness, and density contrast) from Patterson function, is then compared with the measured data in Figure 3a. The good match indicates the effectiveness of our Patterson function analysis method for determining the layer thicknesses, densities, and interface profiles in our complicated multilayer system. The small oscillations between the major peak in the Patterson function result from the termination of the Fourier transformation due to the finite measured range in  $Q$  ( $Q_{\max} = 0.6 \text{ \AA}^{-1}$ ).

**In Operando Observations of ML Lithiation and Delithiation.** The normalized X-ray reflectivity data for the Ge/Ti multilayer sample under potentiostatic control are shown in Figure 4a. The calculated Patterson functions from XRR are shown in Figure 4b. The measurements were performed as the applied electrochemical potential was subsequently held at 0.6, 0.3, 0.02, 0.01, 1, 3, and 3.5 V for a period. The seven-peak pattern in the Patterson function (with 3 positive and 4 negative peaks) observed at the start of cycle begins to diminish at voltages below 0.6 V as the multilayer loses coherence in response to lithiation (as seen previously).<sup>8,24,25</sup> At the same time, the whole pattern gradually moves to larger distances,  $z$ , revealing that the multilayer period is increasing as expected for the lithiation of Ge and suggesting that the whole multilayer increases in thickness. As the potential approaches 0.01 V, the shape of the Patterson function changes and evolves into a distinct three-peak pattern (with 1 positive and 2 negative peaks) that slowly appears and becomes more defined as the potential is held at 0.01 V. Gradually sharper peaks result from the increasing coherence of

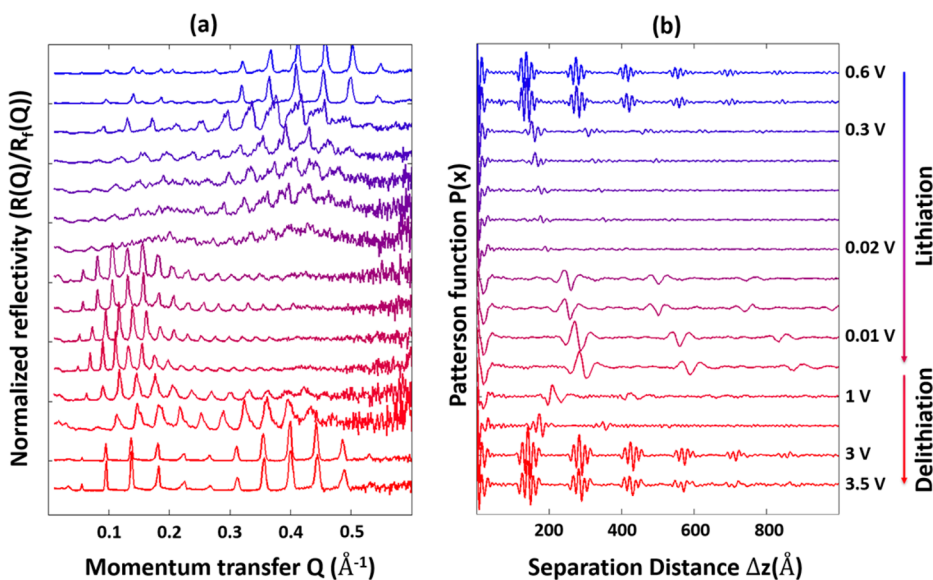


**Figure 4.** (a) *In operando* Fresnel-normalized X-ray reflectivity during electrochemical cycling. (b) The associated Patterson function. The first measurement at each potential is denoted with its applied potential (right-hand side).

the layers. This suggests that the whole film becomes homogeneously lithiated after being held at 0.01 V. Compared with the initial seven-peak pattern, the spacings in the three-peak pattern for the lithiated sample are found at much larger separations, indicating an expansion to more than two times that of the original thickness. The model fit to the Patterson function (Figure 5) at 0.01 V gives numerical results for the

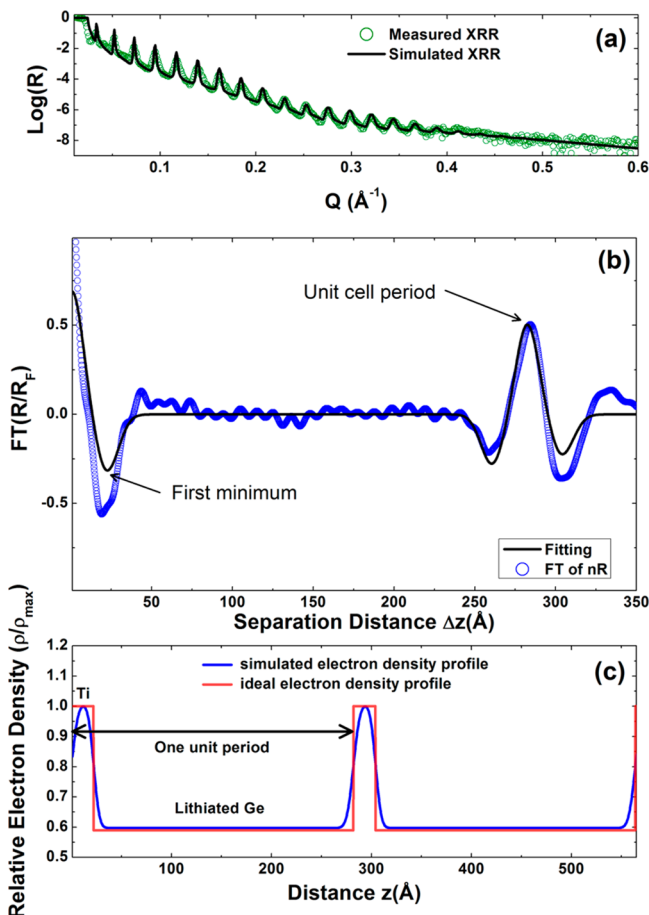


**Figure 5.** Patterson function analysis of the lithiated multilayer structure. (a) Specular X-ray reflectivity data (green circle) of the lithiated Ge/Ti multilayer sample and the calculated XRR signal (black line) using parameters obtained by fitting the observed Patterson function. (b) Calculated Patterson function (blue circle) for the lithiated electrode and the model optimized Patterson function (black line). (c) Ideal model of electron density profile (red line) and optimized density profile obtained from Patterson function analysis (blue line).

average thickness of each layer ( $22.3 \pm 0.2$  Å for the Ti layer and  $259.7 \pm 0.2$  Å for the lithiated Ge layer). The Ti layer thickness is close to the sum of the Ti layer and two  $\text{Ti}_x\text{Ge}$  alloy layers that were found in the original core–shell structure, which indicates that the Ge in  $\text{Ti}_x\text{Ge}$  alloy has been displaced from the original alloy layer and participated in the lithiation process. This implies that the Ti layer in the lithiated structure consists of the original Ti core as well as Ti from the Ge/Ti interfacial alloy coating to form a single Ti layer of increased thickness. At the same time, the lithiated Ge layer has expanded by 228% as expected for its lithiation.

Upon delithiation (0.01–3.5 V), the Patterson function pattern peak heights initially decrease in magnitude at high  $z$ , which is likely due to the loss of coherence between the layers.

The peaks gradually move to smaller heights as the potential is increased, and additional peaks appear in the Patterson functions as the applied potential approaches 1 V, where the Patterson function becomes sharper and more distinct. The reappearance of features in the Patterson function at large separations  $z$  indicates the recovery of coherence between the layers. We also find that the Patterson function reverts to the original seven-peak pattern toward the end of delithiation process, similar to that found for the as-deposited sample, revealing that Ge/Ti alloy observed for the as-deposited film reforms spontaneously upon delithiation. Model fitting of the Patterson function in the delithiated state (Figure 6) verifies

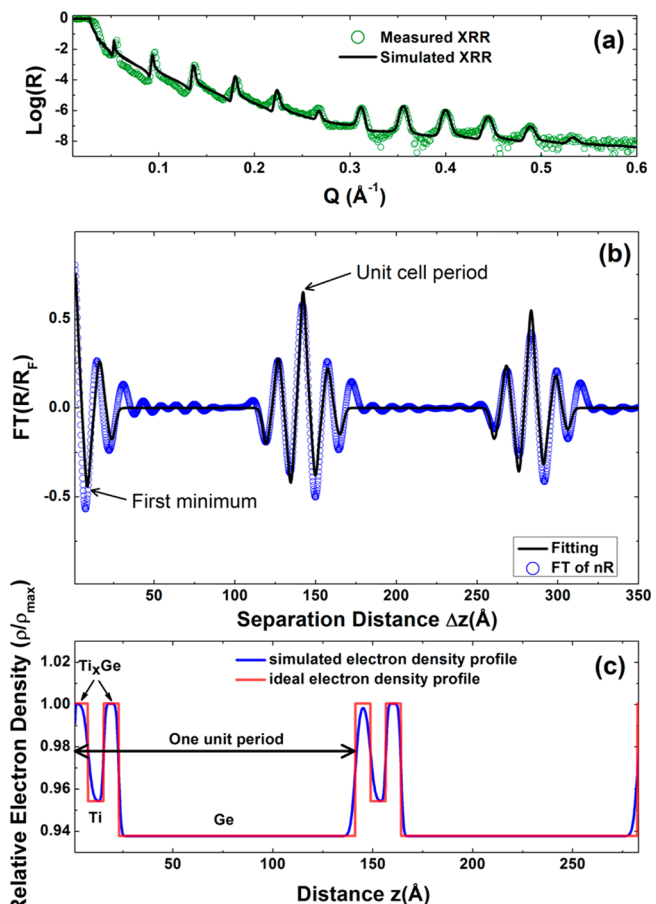


**Figure 6.** Patterson function analysis of the delithiated multilayer structure. (a) Specular X-ray reflectivity data (green circle) of the un lithiated Ge/Ti multilayer sample and the calculated XRR signal (black line) using parameters obtained by fitting the Patterson function. (b) Calculated Patterson function (blue circle) and its fitting curve (black line). (c) Ideal model of electron density profile (red line) and calculated electron density profile from the Patterson function (blue line).

this structure with average thicknesses of  $7.7 \pm 0.1$  Å for Ti,  $118.3 \pm 0.1$  Å for Ge, and  $7.6 \pm 0.1$  Å for the  $\text{Ti}_x\text{Ge}$  alloy layer. The multilayer period of the delithiated structure is within 3% of the as-deposited structure even it had expanded by ~105% upon lithiation. This reveals that the multilayer structure provides a mechanism for high structural reversibility. These results are consistent with previous measurements using Si-based multilayers that also included galvanostatic cycling measurements that revealed functional reversibility for more than 70 cycles.<sup>8</sup> Compared with the original as-deposited state,

the thickness of all layers have increased slightly, which is presumably due to an increase in porosity or trapped lithium within the layers.

In order to better understand the separate processes of the lithiation of the Ge layer and that of the  $\text{Ti}_x\text{Ge}$  alloy, we show the systematic variation of two characteristic spacings found in the Patterson function as a function of applied potential (Figure 7). The first minimum position of the

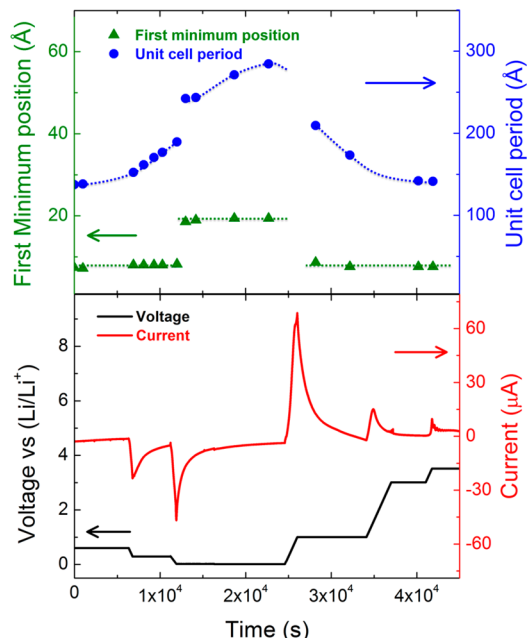
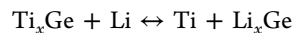


**Figure 7.** Time evolution of the applied voltage (black line) and the *in operando* measurements of the current (red line) as well as associated structural changes derived from the Patterson function analysis, including first minimum (i.e., negative peak) position (green triangles) and the multilayer unit cell period (blue circles). Dotted lines in the top panel are drawn to guide the eye. The first minimum position is associated with the Ti layer thickness, and the period of the Patterson function is related to the thickness of one period in multilayer system.

Patterson function (green triangle) corresponds to the thickness of thinnest layer, which is the central Ti layer in our multilayer system, while the period of the multilayer, which is observed as the maximum of the Patterson function (blue circle), indicates the unit cell thickness. As the applied potential drops from 0.6 to 0.3 V, the unit cell thickness gradually increases while the thickness of Ti layer remains the same, suggesting lithiation of only the Ge layers. Upon decreasing the potential to 0.01 V, the thickness of the Ti layer changes to a value of triple the original thickness and then remains constant. At the same time, the thickness of unit cell also exhibits a small jump, but the Ge layer thickness keeps increasing continuously until it is fully lithiated. The delithiation process shows similar behavior. When the applied potential increases, the Ti layer thickness returns to its original value, while the unit cell thickness decreases gradually until it is fully delithiated. This result reveals that this multilayer structure undergoes two separate reactions. The lithiation and delithiation reactions of the Ge layers occur gradually below 0.6 V (and are presumably strongly influenced by lithium ion transport through the multilayer structure). In addition, the lithiation of the  $\text{Ti}_x\text{Ge}$  alloy core



is a reversible reaction that occurs between 0.3 and 0.01 V. This reaction is better characterized as a conversion reaction due to the need to phase segregate the Ti and Ge components.

The schematic depiction in Figure 8 illustrates the overall changes to the multilayer structure in the first lithiation cycle.

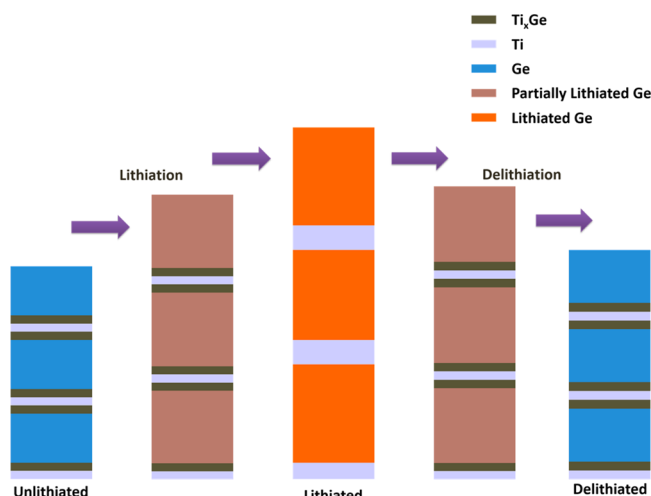


**Figure 8.** Schematic of the structural changes that occur during lithiation and delithiation of the Ge/Ti multilayer structure.

$\text{Ti}_x\text{Ge}$  alloy layers are found in the unlithiated state. Then during lithiation, the Ti and Ge in these alloy layers phase segregate, with the Ti from the surrounding alloy layers nucleating and growing at the  $\text{Ti}_x\text{Ge}/\text{Ti}$  interface to form a thicker pure Ti layer, while the Ge in the alloy layers becomes lithiated along with the pure Ge layers. At this point, the lithiated multilayer structure consists of only two distinct layers per multilayer period: a Ti layer and a lithiated Ge layer. The reversibility of the reaction within the  $\text{Ti}_x\text{Ge}$  alloy layer during delithiation is interesting, as it suggests that Ge diffuses into the Ti layer and re-forms a  $\text{Ti}_x\text{Ge}$  alloy layer upon delithiation. From this observation, we infer that this central alloy layer exhibits multiple functionalities. It is active for lithiation as a conversion material, leading to a phase separation between the Ti and Ge, with the pre-existing Ti layers acting as a nucleation site for the phase segregation and contributing to a portion of the lithium capacity. It also acts as an adhesive that binds the Ge and Ti layers, preventing the working material from cracking or delaminating. Finally, the Ti layer acts as current collector, which ensures electrical conductivity within the multilayer structure.

**Extended Electrochemical Cycling.** Electrochemical stability of these multilayers was tested by lithiation/delithiation cycling in a coin cell (CR2032, 20 mm diameter and 3.2 mm thick) with half-cell geometry (i.e., versus a lithium metal counter electrode). For these tests, the electrodes were deposited on copper foils. The performance of a multilayer having 20 periods of 100 Å Ge and 40 Å Ti layer thicknesses is compared to a thin Ge film with the same overall thickness (2000 Å) (Figure 9). Galvanostatic cycling was performed between 3 and 0.01 V with respect to  $\text{Li}/\text{Li}^+$ . The cycling rate was fixed at a current of 0.32 mA corresponding to a 1 C rate. Both electrodes show a trend of increasing capacity (calculated based on nominal mass of Ge) during the first ~20–50 initial cycles followed by a slow capacity loss. However, the measured

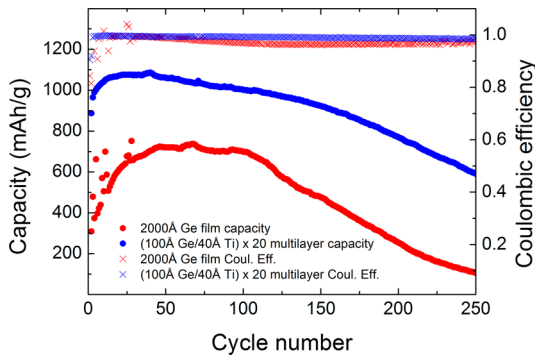


**Figure 9.** Galvanostatic cycling data for a Ge/Ti multilayer in a half-cell with a lithium anode compared to a thin film with same overall Ge thickness grown on copper foil. Solid circles indicate measured capacities, and crosses indicate the associated Coulombic efficiency.

capacity of the multilayer is  $\sim 30\%$  higher than that of the Ge film (1100 mA/g vs 750 mA/g, respectively), and the multilayer capacity retention is substantially above that of the film after 250 charge cycles (600 mA/g vs 100 mA/g, respectively). These results are consistent with the smaller Coulombic efficiency of the Ge thin film with respect to the multilayer. These results reveal that the multilayer architecture has superior electrochemical properties with respect to a comparable single-layer Ge thin film.

## CONCLUSIONS

These studies demonstrate that a Ti/Ge multilayer structures exhibits high structural reversibility during lithiation/delithiation cycles. The choice of Ti for these structures, which was originally chosen as conductive current collector, exhibited additional unexpected functions. The structural changes that take place during lithiation of these multilayers were observed by *in operando* X-ray reflectivity and understood through analysis of the associated Patterson functions. At the (unlithiated) as-deposited state, Ti and Ge spontaneously form an alloy layer  $Ti_xGe$  at the interface between the Ti and Ge layers. While the Ge layers begin to lithiate below 0.6 V, the Ti/Ge alloy layer phase separates into Ti and Ge at potentials below 0.3 V. At that point, the  $Ti_xGe/Ti/Ti_xGe$  core transforms into single Ti layer with a thickness of  $\sim 3$ -fold larger than the original Ti layer. During delithiation, the Ge spontaneously alloys with Ti leading to the reversible formation of  $Ti_xGe$  alloy layers. Consequently, the alloying of Ti with Ge also acts as an adhesive material which helps stabilize the morphology of the active Ge layer to prevent cracking, delamination, and pulverization. The success of this strategy is demonstrated in the improved capacity and capacity retention of the multilayer structure with respect to a Ge film with equivalent thickness. The present observations provide a new strategy for addressing the dramatic (up to 2.3-fold) volume changes that occur during the lithiation/delithiation cycles of Ge and opens up a new route for stabilizing the lithiation of group IV intermetallics.

## AUTHOR INFORMATION

### Corresponding Author

\*E-mail: [Fenter@anl.gov](mailto:Fenter@anl.gov) (P.F.).

### ORCID

Andrew A. Gewirth: [0000-0003-4400-9907](https://orcid.org/0000-0003-4400-9907)

Michael J. Bedzyk: [0000-0002-1026-4558](https://orcid.org/0000-0002-1026-4558)

Paul Fenter: [0000-0002-6672-9748](https://orcid.org/0000-0002-6672-9748)

### Notes

The authors declare no competing financial interest.

## ACKNOWLEDGMENTS

This research was supported by the Center for Electrochemical Energy Science, an Energy Frontier Research Center funded by the U.S. Department of Energy, Office of Science, Office of Basic Energy Sciences, under Contract DE-AC02-06CH11357. Research at the Advanced Photon Source (Station 33BM-C) at Argonne National Laboratory was also supported by DOE. A portion of this work was performed at Northwestern University facilities including X-ray Diffraction Facility and the NUANCE Center that are supported by the MRSEC program through NSF Contract DMR-1121262.

## REFERENCES

- Graetz, J.; Ahn, C. C.; Yazami, R.; Fultz, B. Nanocrystalline and Thin Film Germanium Electrodes with High Lithium Capacity and High Rate Capabilities. *J. Electrochem. Soc.* **2004**, *151* (5), A698–A702.
- Laforge, B.; Levan-Jodin, L.; Salot, R.; Billard, A. Study of Germanium as Electrode in Thin-Film Battery. *J. Electrochem. Soc.* **2008**, *155* (2), A181–A188.
- Zhang, W. M.; Hu, J. S.; Guo, Y. G.; Zheng, S. F.; Zhong, L. S.; Song, W. G.; Wan, L. J. Tin-Nanoparticles Encapsulated in Elastic Hollow Carbon Spheres for High-Performance Anode Material in Lithium-Ion Batteries. *Adv. Mater.* **2008**, *20* (6), 1160–1165.
- Wang, F.; Wu, L. J.; Key, B.; Yang, X. Q.; Grey, C. P.; Zhu, Y. M.; Graetz, J. Electrochemical Reaction of Lithium with Nanostructured Silicon Anodes: A Study by *in-Situ* Synchrotron X-Ray Diffraction and Electron Energy-Loss Spectroscopy. *Adv. Energy Mater.* **2013**, *3* (10), 1324–1331.
- Yang, L. C.; Gao, Q. S.; Li, L.; Tang, Y.; Wu, Y. P. Mesoporous Germanium as Anode Material of High Capacity and Good Cycling Prepared by a Mechanochemical Reaction. *Electrochim. Commun.* **2010**, *12* (3), 418–421.
- Wang, J. Z.; Du, N.; Song, Z. Q.; Wu, H.; Zhang, H.; Yang, D. R. Synthesis of Sige-Based Three-Dimensional Nanoporous Electrodes for High Performance Lithium-Ion Batteries. *J. Power Sources* **2013**, *229*, 185–189.
- Chan, C. K.; Peng, H. L.; Liu, G.; McIlwrath, K.; Zhang, X. F.; Huggins, R. A.; Cui, Y. High-Performance Lithium Battery Anodes Using Silicon Nanowires. *Nat. Nanotechnol.* **2008**, *3* (1), 31–35.
- Fister, T. T.; Esbenshade, J.; Chen, X.; Long, B. R.; Shi, B.; Schleputz, C. M.; Gewirth, A. A.; Bedzyk, M. J.; Fenter, P. Lithium Intercalation Behavior in Multilayer Silicon Electrodes. *Adv. Energy Mater.* **2014**, *4* (7), 1301494.
- Cao, C.; Steinruck, H. G.; Shyam, B.; Stone, K. H.; Toney, M. F. In Situ Study of Silicon Electrode Lithiation with X-Ray Reflectivity. *Nano Lett.* **2016**, *16* (12), 7394–7401.
- Wang, Z. G.; Gu, M.; Zhou, Y. G.; Zu, X. T.; Connell, J. G.; Xiao, J.; Perea, D.; Lauhon, L. J.; Bang, J.; Zhang, S. B.; Wang, C. M.; Gao, F. Electron-Rich Driven Electrochemical Solid-State Amorphization in Li-Si Alloys. *Nano Lett.* **2013**, *13* (9), 4511–4516.
- Conwell, E. M. Properties of Silicon and Germanium. *Proc. IRE* **1952**, *40* (11), 1327–1337.
- Fuller, C. S.; Severiens, J. C. Mobility of Impurity Ions in Germanium and Silicon. *Phys. Rev.* **1954**, *96* (1), 21–24.
- Obrovac, M. N.; Chevrier, V. L. Alloy Negative Electrodes for Li-Ion Batteries. *Chem. Rev.* **2014**, *114* (23), 11444–11502.
- Fister, T. T.; Long, B. R.; Gewirth, A. A.; Shi, B.; Assoufid, L.; Lee, S. S.; Fenter, P. Real-Time Observations of Interfacial Lithiation in a Metal Silicide Thin Film. *J. Phys. Chem. C* **2012**, *116* (42), 22341–22345.
- Chason, E.; Mayer, T. M. Thin Film and Surface Characterization by Specular X-Ray Reflectivity. *Crit. Rev. Solid State Mater. Sci.* **1997**, *22* (1), 1–67.

- (16) Parratt, L. G. Surface Studies of Solids by Total Reflection of X-Rays. *Phys. Rev.* **1954**, *95* (2), 359–369.
- (17) Als-Nielsen, J.; McMorrow, D. *Elements of Modern X-Ray Physics*; John Wiley & Sons: Hoboken, NJ, 2011.
- (18) Owejan, J. E.; Owejan, J. P.; DeCaluwe, S. C.; Dura, J. A. Solid Electrolyte Interphase in Li-Ion Batteries: Evolving Structures Measured in Situ by Neutron Reflectometry. *Chem. Mater.* **2012**, *24* (11), 2133–2140.
- (19) Hirayama, M.; Sonoyama, N.; Ito, M.; Minoura, M.; Mori, D.; Yamada, A.; Tamura, K.; Mizuki, J.; Kanno, R. Characterization of Electrode/Electrolyte Interface with X-Ray Reflectometry and Epitaxial-Film  $\text{LiMn}_2\text{O}_4$  Electrode. *J. Electrochem. Soc.* **2007**, *154* (11), A1065–A1072.
- (20) Als-Nielsen, J. Synchrotron X-Ray Studies of Liquid-Vapor Interfaces. *Phys. A* **1986**, *140* (1–2), 376–389.
- (21) Warren, B. E. *X-Ray Diffraction*; Courier Corporation: North Chelmsford, MA, 1969.
- (22) Astaf'ev, S. B.; Shchedrin, B. M.; Yanusova, L. G. Estimation of the Characteristic Parameters of the Multilayered Film Model Using the Patterson Differential Function. *Crystallogr. Rep.* **2010**, *55* (1), 127–135.
- (23) Thomas, O.; Dheurle, F. M.; Delage, S. Some Titanium Germanium and Silicon-Compounds - Reaction and Properties. *J. Mater. Res.* **1990**, *5* (7), 1453–1462.
- (24) Evmenenko, G.; Fister, T. T.; Buchholz, D. B.; Li, Q.; Chen, K.-S.; Wu, J.; Dravid, V. P.; Hersam, M. C.; Fenter, P.; Bedzyk, M. J. Morphological Evolution of Multilayer Ni/NiO Thin Film Electrodes During Lithiation. *ACS Appl. Mater. Interfaces* **2016**, *8* (31), 19979–19986.
- (25) Fister, T. T.; Hu, X. Y.; Esbenshade, J.; Chen, X.; Wu, J. S.; Dravid, V.; Bedzyk, M.; Long, B.; Gewirth, A. A.; Shi, B.; Schleputz, C. M.; Fenter, P. Dimensionally Controlled Lithiation of Chromium Oxide. *Chem. Mater.* **2016**, *28* (1), 47–54.